Chemical Engineering Journal Advances 15 (2023) 100503

Contents lists available at ScienceDirect

Chemical Engineering Journal Advances

journal homepage: www.sciencedirect.com/journal/chemical-engineering-journal-advances

Application of the distribution of relaxation time method in electrochemical analysis of the air electrodes in the SOFC/SOEC devices: A review

Mitra Ghamarinia [a], Alireza Babaei [a,*], Cyrus Zamani [a], Hamed Aslannejad [b]

[a] School of Metallurgy and Materials Engineering, College of Engineering, University of Tehran, Tehran, Iran
[b] Copernicus Institute of Sustainable Development, Utrecht University, Utrecht, the Netherlands

ARTICLE INFO

Keywords:
Solid oxide cells
Electrochemical impedance analysis
Distribution of relaxation time method
Air electrodes

ABSTRACT

Understanding electrochemical sub-processes occurring at solid oxide cells (SOCs) components, mainly air electrodes, is of high importance since they play a key role in improving the performance of SOC devices and their durability. Among various performance analysis methods, electrochemical impedance spectroscopy (EIS) is the most used one in studies. However, analyzing and interpreting EIS data have always been considered as a challenge given the fact that the information provided by the common approach of complex non-linear least square (CNLS) method is limited. Viewed in this sight, the distribution of relaxation time (DRT) approach has gained considerable attention in recent years as a potential approach to analyze EIS measurement results. This study aims at reviewing recent publications that used the DRT method to deconvolute the EIS data and at pathing the way to use DRT methodology and incorporate its results. Studies are focused on six categories of commonly used air electrodes, namely LSCF-based, LSM-based, lanthanide nickelates-based, BSCF-based, and double perovskite-based electrodes, and less-common-used ones.

1. Introduction

A solid oxide cell (SOC) is an all-solid-state electrochemical energy conversion device that has drawn broad attention among renewable energy conversion community to compensate for the intermittency of the most abundant renewables energy resources such as photovoltaic solar cells and wind turbines [1–4]. SOCs can operate in either electrolysis cell (EC, so SOEC) or fuel cell (FC, so SOFC) mode. In the SOEC mode, electricity is converted to chemical energy stored in fuels such as CO and H_2, and in the SOFC mode, electricity is generated through oxidizing chemical fuels (such as Hydrogen, Methane) [2,5–8]. Air electrodes are one of the crucial cell components and they need to meet some pivotal requirements, including appropriate thermal expansion coefficient with other cell components such as electrolyte and interconnects, high electronic conductivity (greater than 100 S m^{-1}), sufficient porosity for oxygen gas diffusion towards the electrode surface as well as the electrode/electrolyte interface, and, last but not least, high catalytic activity for the oxygen reaction namely oxygen reduction reaction (ORR) in the SOFC and oxygen evolution reaction (OER) in the SOEC mode [9–14]. Among all of these required characteristics, the catalytic activity of the electrode turns out to be the most important and challenging parameter due to the high activation energy of the oxygen reaction (reaction 1), especially at intermediate and low-temperature ranges.

$$\frac{1}{2}O_2\ (g) + 2e' + V_{O^{\cdot\cdot}} \xleftrightarrow{reversible} O_{O^{\times}} \quad (1)$$

In the equation, $V_{O^{\cdot\cdot}}$ is an oxygen vacancy and $O_{O^{\times}}$ is an oxygen ion at a normal oxygen lattice site [15,16]. This equation involves some sub-processes. For instance, in the fuel cell mode, the sub-processes include: 1. oxygen gaseous diffusion; 2. oxygen molecules adsorption on adsorption sites; 3. oxygen molecules dissociation to monoatomic oxygen species; 4. oxygen species diffusion through surface to active sites; 5. partial reduction of oxygen species; and 6. oxygen species combination with an oxygen vacancy [17]. In an oxygen electrode, each of these sub-processes can control the whole reaction mechanism by being the rate-limiting step, and, therefore, it can affect the polarization resistance of the electrode and influence on the power or hydrogen generation of SOFC/SOEC devices [18,19]. Accordingly, having a good insight into the physicochemical phenomena of the air electrode is

* Corresponding author.
E-mail address: alireza.babaei@ut.ac.ir (A. Babaei).

https://doi.org/10.1016/j.ceja.2023.100503

Available online 5 May 2023
2666-8211/© 2023 The Author(s). Published by Elsevier B.V. This is an open access article under the CC BY-NC-ND license (http://creativecommons.org/licenses/by-nc-nd/4.0/).

vitally important. In this regard, the distribution of relaxation time (DRT) method has gained extensive attention in recent years. There have been many research analyzing the performance of various oxygen electrodes using the DRT approach as the main or additional methodology. This paper aims to teach readers about the ways by which DRT is applied in various papers, their approach towards its interpretation, and the method's high potential in the field of electrochemistry. It is worth mentioning that we tried to mention papers whose approach was more comprehensive and was more trustworthy with regard to understanding electrochemical processes. The review is done by considering $La_{0.6}Sr_{0.4}Co_{0.}Fe_{0.8}O_{3-\delta}$ (LSCF), (Ba, Sr)(Co, Fe)O_3 (BSCF), $La_{0.8}Sr_{0.2}MnO_3$ (LSM), lanthanide nickelate oxides, and double perovskite electrodes since they are mostly employed as the common oxygen electrodes in SOEC/SOFC technologies. Besides, other less-applied electrode materials are also discussed.

2. Electrochemical analysis

2.1. Electrochemical impedance spectroscopy

To improve the performance of a SOC system and to increase its durability, understanding the processes taking place in its components is crucially important. In addition to that, selecting proper materials with optimized microstructures is of great importance [10,20]. Electrochemical impedance spectroscopy (EIS) methodology is one of the mostly used approaches to study electrode/electrolyte processes in electrochemical energy convertor devices by monitoring the dynamics of these systems. It is concluded that by adequate measuring steps using this method, all collectible information of the system under study can be gained [21]. The information given by EIS is mostly revealed by some common representations such as the Nyquist, Bode, current density-voltage, and anodic/cathodic polarization curves [22]. Among all of the mentioned graphical representations, the Nyquist plots are the most employed ones in which the real part of the impedance is plotted versus the imaginary part of the impedance and appears in the shape of single or multiple arcs. These plots are considered to be highly useful in investigating the impedance parameters. Electrical equivalent circuits, introduced by the well-established complex non-linear least square (CNLS) method, have been commonly used to analyze the impedance responses; which should be chosen based on an intuitive understanding of the physical and chemical properties of the investigated system [23]. However, since the applied circuits are analogs, only some limited information about the electrochemical phenomena can be extracted. Accordingly, the complete interpretation of the EIS response remains to be fully implemented. Considering the multistage nature of electrode reactions, EIS generated data will remain difficult to interpret especially in complex systems with several numbers of sub-processes due to the overlapped various electrochemical phenomena [24–27].

2.2. Distribution of relaxation times

Applying the DRT method to SOCs with the aim of system performance study was firstly conducted by researchers working at Karlsruhe Institute of technology in 1999 [28], and then other researchers, mainly Boukamp [29–32], Zhang et al. [22,32–35], Klotz et al. [21,36–39], Hahn et al. [40,41], Gavrilyuk et al. [42,43], started reintroducing the method, improving it, and making it known as a popular method [26]. The distribution of relaxation times is a potential superseded or an excessive helpful method – as it is applied in many studies– for the equivalent circuit model selection by which an accurate pre-identification and deconvolution of impedance response can be gained. The method is applied by calculating the DRT function which can be done through various software packages such as DRT tools [32] and RAVDAV [44] or by online services such as RelaxIS DRT [45]. As it has been mentioned by Schichlein et al. [28], the pioneers of this method, DRT is mainly applied based on obtained experimental data in order to produce a mathematical model instead of physical laws which were used for equivalent circuit models . It should be noted that the physical processes could then be correlated to the model parameters. In a Nyquist plot, each point is related to the impedance at one frequency and the DRT function transforms these points from the frequency-domain to the relaxation time-domain called τ; which is inversely related to the frequency, based on the equation $\tau = \frac{1}{2\pi f}$ [23, 30]. DRT impedance is an equivalent Voigt circuit with an infinite number of elements explained by a Fredholm integral equation which contains the distribution function. In fact, if a Voigt circuit, with N R_k/C_k elements that have N time constant τ_k, is used to fit into impedance data, each R_k can distinctly be plotted as a function of the corresponding τ_k. Therefore, if a continuous variation of R(τ) is considered, instead of individual values of R_k vs. τ_k, the distribution function is then made [45]. Inverting the data from the frequency domain to the τ-domain requires solving the below expression, Eq. (1), the Fredholm integral; R_∞ is the ohmic resistance, $\gamma(ln\tau)$ is the DRT function reporting the time relaxation characteristics of the system [30].

$$Z_{DRT} = R_\infty + \int_{-\infty}^{\infty} \frac{\gamma(\ln\tau)}{1 + i2\pi f\tau} d\ln\tau \quad (1)$$

Various techniques have been developed to solve this equation and invert the impedance data to the τ-domain such as Fourier Transform [37,46–48], Tikhonov Regularization [32,49–55], and Maximum entropy [56,57]. What is important in all these methods is that they need the adjustment of a special parameter so that an acceptable DRT function could be achieved. For instance, in the case of Tikhonov Regularization, which is the most-used one, the adjustment of a regularization parameter (λ) is necessary as it is the most important parameter affecting the shape of DRT graphs. In fact, the parameter defines the smoothness of the achieved spectra. While choosing an appropriate λ is vital to obtain a reliable DRT, no exact method has been introduced for finding the parameter. As it is stated by Engl et al. [58], who examined the issue from a mathematical point of view, there is no black-box procedure for finding λ, and, most presumably, it will never exist. Until now, some papers have been published on explaining various mathematical ways of determining an optimum amount of λ automatically [34,59–63]. Even there are some groups suggesting to find DRT functions without any need for regularization parameter [22,43]. All in all, when reviewing papers using DRT as a method for analyzing their EIS data, we see that few researchers have explained their method towards selecting an optimum λ. On top of this, in our opinion, confirmed by Ivers-Tiffée's team who have worked a great deal on DRT [64], the proposed mathematical methods might not be accurate and users need to be cautious when applying them. What highly works to our experience is analyzing the DRT results of a sample under varying operating conditions such as temperature, oxygen partial pressure, time, current density, and the loading of infiltrated materials. In fact, when testing different values of λ for a sample under various operating conditions, a user can see that there are some peaks which change randomly while there are others which are stable with some minor changes. The later ones are most likely the peaks with a physical meaning for which the user should search about the story behind. The important point here is to consider the SAME amount of λ for a sample once the optimum λ is found. To give a cue for considering a starting value for finding λ, we can say that papers mostly test the range of $1–10^{-10}$. Higher amounts of λ generates fewer peaks and fewer information; and if it is too large, some peaks might be ignored. On the other side, lower amounts of λ, heighten peaks' resolution and generate more peaks; yet, if it is too small, false peaks may be observed, resulting to over-interpretation. Finally, the most important point here is to get the EIS data with the highest quality, having as few noises and errors as possible. This is because any noise or an error can deviate DRT results. Kramers-Kronig approach is a good way for testing the quality of EIS data [38,64–67,30,36,68].

Finally, it should be mentioned that in a DRT spectrum, in which the distribution function of relaxation times is plotted versus the time constant, there is a set of peaks whose positions describe the major time constants of the electrochemical system. The area under each individual peak is corresponding to the polarization resistance of a sub-process in the electrochemical response by which it is possible to resolve the impedance data and comprehend the physicochemical processes of complex electrochemical systems.

3. Electrochemical characterization of air electrodes for SOC

3.1. LSCF-based electrodes

The most studied air electrode for low to intermediate temperature SOCs is lanthanum strontium cobalt ferrite ($La_{0.6}Sr_{0.4}Co_{0.2}Fe_{0.8}O_{3-\delta}$, LSCF), which is mainly used for its excellent mixed ionic and electronic conductivity (MIEC) [69–71]. Owing to its incredible popularity, in comparison with other electrode materials, most of the DRT-based studies have chosen this electrode material as their case of study. In a comprehensive study, Chen et al. [17] studied the electrocatalytic activity of multiphase catalyst-coated LSCF cathode, which is said not only is it applicable to SOFCs, but also to other energy conversion and storage systems such as high-temperature SOECs and metal-air batteries. The multiphase catalyst contains $BaCoO_{3-x}$ (BCO) and $PrCoO_{3-x}$ (PCO) nanoparticles and a $PrBa_{0.8}Ca_{0.2}Co_2O_{5+\delta}$ thin film, which significantly improved the ORR at the cathode. For instance, the polarization resistance dropped from 2.57 to 0.312 Ω.cm^2 at 600 °C. To understand the electrochemical behavior of the cathode, two sets of DRT analysis were applied in two different situations – the first set: constant oxygen partial pressure and various temperatures (600, 650, 700, 750 °C) and the second set: constant temperature (750 °C) and various oxygen partial pressures (1, 0.8, 0.6, 0.4, and 0.21 atm). Three distinct peaks were observed in each plot of both two sets, being the low frequency, intermediate frequency, and high frequency. The low-frequency peak (0.1–10 Hz) was ascribed to the gas diffusion in the cathode because it was not sensitive to temperature but to oxygen partial pressure. The intermediate-frequency peak was highly dependent on both temperature and oxygen-partial pressure; hence, it was associated with oxygen surface exchange, oxygen adsorption/desorption, dissociation, and/or surface transport processes. In addition, it was claimed that the high-frequency peaks were representative of one or more charge transfer processes across the interfaces, which had thermal activations and were insensitive to oxygen partial pressure. For a more accurate study, peaks were analyzed by the general relationship between polarization resistance of individual electrode processes and oxygen partial pressure($R_p = R_P^0 (P_{O_2})^{-n}$); in which the exponent n is the slope of the polarization resistance as a function of oxygen partial pressure. This relation is typically used to determine the rate-limiting step given that each value of n is illustrative of a sub-process of oxygen reduction reaction happening at the air electrode. Values of 0, 0.25, 0.5, and 1 are the most common values of n reported in the literature although intermediate values are also reported [72,73]. In the aforementioned study, the n = 1.16 showed that the low-frequency peaks were related to mass transport, the n = 0.516 indicated that the intermediate-frequency peaks were attributed to dissociation of O_2 into $2O_{ads}$, and the n of 0.023 suggested that the high-frequency peaks corresponded with O^{2-} transfer across the electrode/electrolyte interface. As it is shown in Fig. 1, DRT analysis in various testing times revealed that the intermediate-frequency peak (P2) dominated the whole resistance of the bare electrode. It can be observed that applying the multiphase catalyst highly improved the oxygen exchange process. This extraordinary impact originated from more oxygen exchange and oxygen transport paths introduced by the very uncommon oxygen vacancy arrangement of the multiphase catalyst. What is more, according to the analysis of DRT results of the multiphase-coated LSCF in Fig. 1, the resistance

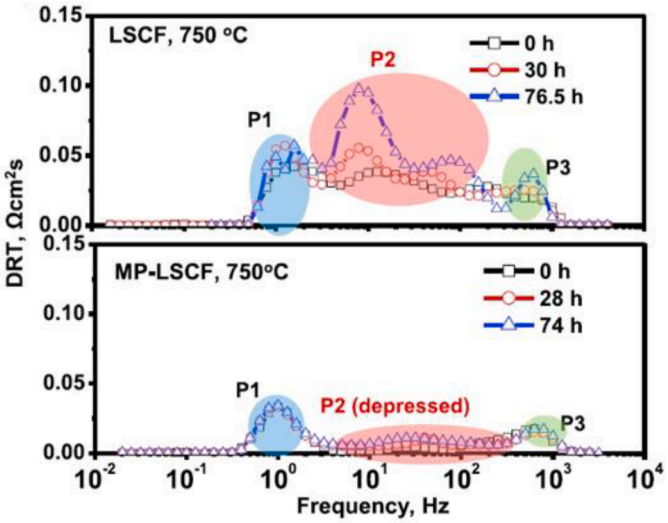

Fig. 1. DRT graphs of pure LSCF and multiphase coated LSCF (MP-LSCF) in different testing times, under OCV conditions at 750 °C [17].

corresponding to intermediate-frequency peaks remained unchanged during the testing time indicating that the surface Sr segregation experienced a significant decrease because of the introduction of catalysts.

Pan et al. [74] employed LSCF as the air electrode of SOEC and analyzed the effects of the interface between LSCF and electrolyte (yttria-stabilized zirconia or YSZ and gadolinium doped ceria or GDC) on the short-term stability during 1 A cm^{-2} electrolysis at 800 °C for 264 h through examining various types of half-cells; configurations were YSZ | LSCF (sintered at 800 °C), YSZ | LSCF (sintered at 1000 °C), GDC | LSCF (sintered at 1000 °C), YSZ | porous GDC| LSCF (sintered at 1000 °C), and YSZ | dense GDC | LSCF (sintered at 1000 °C). It was deduced that the half cell with YSZ electrolyte, dense GDC interlayer, and LSCF electrode sintered at 1000 °C showed the best performance among all half-cells since there was no $SrZrO_{3\ s}$ phase formation, no delamination in the electrode, and less degradation rate of R_p in it. To detect the possible degradation mechanism in this half-cell, the DRT approach was applied. By means of which it would be possible to follow the changes of electrochemical responses during the electrolysis test under 1 A cm^{-2} for 264 h at 800 °C. DRT results (Fig. 2) showed one main peak with a summit frequency of 100 Hz and two other small peaks at the beginning of the test. The summit frequency of the main peak reached 60 Hz and its height increased after 96 h after which its height gradually increased. The peaks were most likely associated with electron and oxygen ion transfer at 10^3 Hz, mass transfer at 10^2, and gas diffusion at 10 Hz. It was understood that the mass transfer process (oxygen adsorption/desorption, dissociation/association, and diffusion), which was attributed to the main peak, played a key role in the degradation phenomenon. In addition, it was claimed that the recrystallization and agglomeration of the LSCF particles may have changed the summit frequency and height of the main peak.

In another study, Nadeem et al. [75] examined the electrochemical performance of the LSCF cathode electrode infiltrated with lead oxide (PbO) for SOFC devices. In this work, DRT analysis revealed three distinct peaks, namely charge transfer, oxygen incorporation, and oxygen gas diffusion. After the introduction of 5.88 wt% PbO onto the electrode surface, the integral area corresponding to charge transfer and oxygen incorporation sub-processes decreased, which suggested the acceleration of these two steps. It was also mentioned that the gas diffusion process slightly slowed down which was caused by reduction of pore sizes. In our previously done study [25], we infiltrated various loadings of Ruddlesden-Popper-structured $La_2NiO_{4+\delta}$ (LNO) nanoparticles onto the surface of LSCF as a cathode of intermediate to low-temperature SOFCs. Then we examined the ORR mechanism

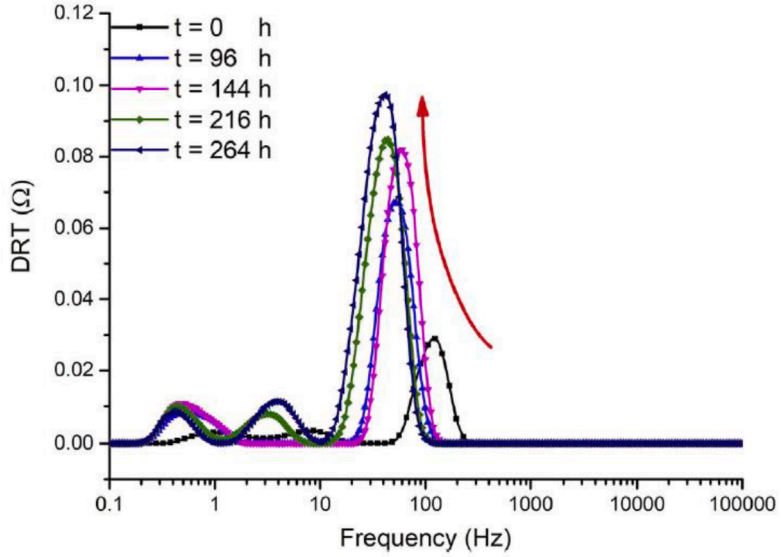

Fig. 2. DRT results of the half-cell containing YSZ electrolyte, dense GDC interlayer, and LSCF electrode sintered at 1000 °C during the electrolysis test under 1 A cm^{-2} for 264 h at 800 °C [17].

through electrochemical analysis. The DRT approach employed for non-infiltrated electrodes identified four different peaks and hence four different sub-processes. By considering the trend of peaks, from low to high frequencies, four sub-processes were identified; gas diffusion, oxygen surface exchange, oxygen ion transfer across the cathode/electrolyte interface, and electron transfer between the cathode and the

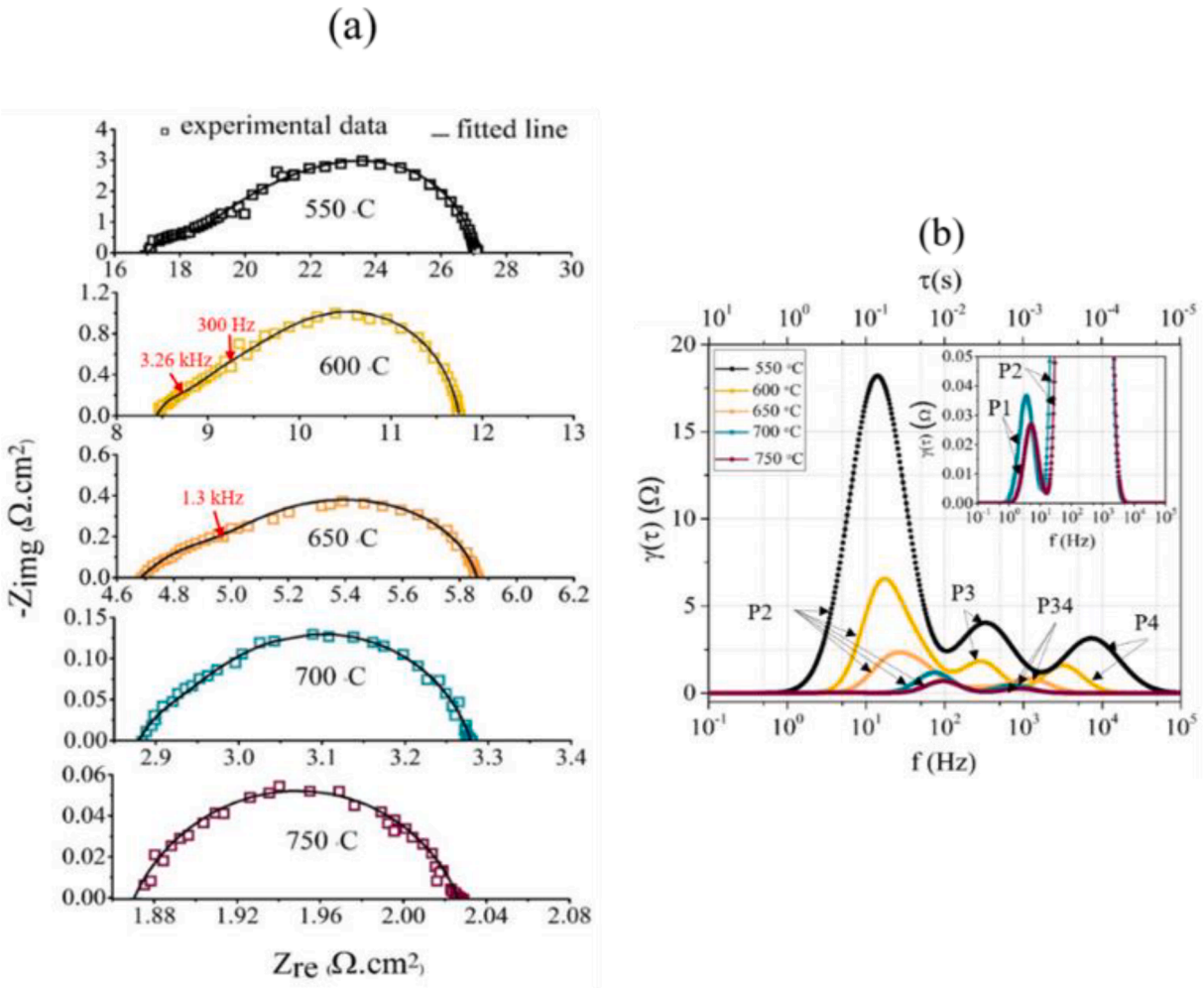

Fig. 3. (a) EIS graph and (b) corresponding DRT spectra for bare LSCF electrode at 550–750 °C [25].

current collector. As shown in Fig. 3b, the gas diffusion peak (P1) only appeared in higher temperatures (700 and 750 °C), while the oxygen surface exchange peak (P2) was separately visible in all temperatures, showing a remarkable thermal activation in comparison to other peaks. Regarding charge transfer peaks, P3: oxygen ion transfer and P4: electron transfer, it can be seen that they merged by elevating the temperature. By analyzing the EIS graphs of Fig. 3a, it is understood that there was a slight change in the shape of arcs by increasing the temperature. Thanks to the DRT approach, the reason behind these changes was made clear. Considering the EIS graphs of the temperatures of 600 and 650 °C in Fig. 3a, for instance, the summit frequency of the merged charge transfer peak at 650 °C (P34, 1.3 kHz) was between the summit frequency of the oxygen ion transfer peak (P3, 0.3 kHz) and electron transfer (P4, 3.26 kHz) at 600 °C. That corroborated the changes in the Nyquist plots. Furthermore, the depression of merged charge transfer peak (P34) at 650, 700, and 750 °C was mostly attributed to the increase of oxygen vacancies concentration in LSCF and hence reduced resistance of oxygen ion transfer. Via the increase in temperature, there is a transition in the electronic conduction of LSCF material from semiconducting to metallic and its maximum conductivity takes place around 600 °C. It was observed that LNO infiltration significantly decreased the integral area of the peaks associated with oxygen surface exchange and oxygen ion transfer in both high and low temperatures. That attributed to high surface exchange (k) and bulk oxygen diffusion (D) coefficients of LNO material. Even so the area under the electron transfer peak decreased at 550 °C, it slightly increased at higher temperatures. This result stemmed from the fact that LNO has lower electronic conductivity rather than LSCF, and also it shows a transition in electronic conduction and achieves its maximum conductivity around the temperature of 450 °C which is near 550 °C. However, after the infiltration of higher amounts of LNO material, its negative impact on the electron transfer process was mitigated. It should be noticed that, there was not a noticeable change in the area under the gas diffusion peak through LNO infiltration.

Soltanizade et al. [76] used DRT graphs to gain some insights into the electrochemical reactions taking place at the LSCF air electrode which was infiltrated with three distinct nano catalysts including Ag-ceria, Co-ceria, and $Ba_{0.5}Sr_{0.5}Co_{0.8}Fe_{0.2}O_3$. As for non-infiltrated electrodes at 500 and 700 °C and under OCV conditions, the DRT function contained one peak with a hillside, which was associated with the Gerischer element. Since an identical trend was seen in EIS and DRT graphs of the bare electrode at 500 and 700 °C, it was claimed that it had similar electrochemical characteristics in the temperature range of 500–700 °C. Based on the DRT results, they introduced *RLG* equivalent circuit for the bare electrode. Infiltration of the nano catalysts changed the DRT graph where no sign of Grischer element was visible and two new peaks were identified at low and high frequencies, which were related to the adsorption and dissociation of oxygen species at low frequencies and charge transfer processes at high frequencies. The chosen equivalent circuit for infiltrated electrodes consisted of two constant phase elements paralleled with resistance $(RL(R_1Q_1)(R_2Q_2))$. The impact of each nano catalyst on the DRT graph was different.

3.2. LSM-based electrodes

Strontium-doped lanthanum manganite perovskite oxide (LSM) is considered to be one of the most common air electrodes of high-temperature SOCs. Acceptable catalytic activity for ORR, high electronic conductivity, great chemical and thermal stability, and also compatibility with the widespread used YSZ electrolyte at intermediate temperatures [77–80] are the main characteristics of LSM. Song et al. [81] studied combined LSM with the conventional YSZ as the air electrode of SOEC and added gold nanoparticles to it for CO_2 electrolysis at 800 °C. Through electrochemical analysis – J/V curve assessment, chronoamperometric test, and EIS measurement – it was concluded that introducing gold nanoparticles remarkably enhanced the performance of the LSM-YSZ anode. Employing the DRT method by fitting the impedance curves with an equivalent circuit model for the full-cells (YSZ-NiO support, YSZ-NiO fuel electrode, YSZ electrolyte, and LSM-YSZ air electrode) revealed six distinct peaks, which had four peaks corresponding to four elementary processes at the air electrode, plus two distinct peaks corresponding to two elementary processes at the fuel electrode. The sub-processes taking place at the air electrode were oxygen anions transport through the electrolyte, oxygen species diffusion from the electrolyte to the air electrode surface, oxygen evolution, and oxygen gas diffusion. CO_2 electro-reduction at the triple-phase boundaries and CO_2 diffusion at the fuel electrode were sub-processes happening at the fuel electrode. It was reported that although all resistances associated with the air electrode were decreased after adding gold nanoparticles to LSM-YSZ, the peak corresponding to the oxygen evolution process had the greatest depression. Through further physicochemical characterizations – XRD, XPS, and oxygen temperature-programmed desorption – it was understood that gold nanoparticles changed neither the electronic property nor the number of oxygen vacancies of the air electrode. However, individual investigation of the electrochemical performance of the Au-infiltrated LSM and YSZ components showed that gold nanoparticles improved both ohmic and polarization resistances of both YSZ+Au and LSM+Au electrodes. In case of LSM+Au, the high electronic conductivity of gold improved electrode resistances and consequently, the peak related to the oxygen evolution process depressed through accelerated electron transfer of oxygen ions. Furthermore, the newly generated triple-phase boundaries, as the new active sites for the oxygen evolution process, were known as the reason behind the improved resistances of the YSZ+Au electrode. Akbari and Babaei [77] used DRT as an approach to analyze the electrochemical response of LNO-infiltrated LSM air electrodes under SOFC and SOEC modes. First of all, they applied DRT analysis to non-infiltrated LSM under open circuit voltage conditions at 800 °C and compared the DRT curve with the corresponding Bode plot to show how DRT can distinguish between the peaks. As shown in Fig. 4a, despite the indistinct separation of the Bode plot, the DRT profile individualized the two peaks; namely low and high-frequency peaks. DRT results of the anodic polarization behavior of the air electrode under -200 mA cm^{-2} at 800 °C for 10 h showed that for the non-infiltrated electrode, the low-frequency peak shifted toward lower frequencies which lead to the separation of the two arcs (Fig. 4b). Although there was no significant change in the height of the high-frequency peak, the height of the low-frequency one was increased which was more affected by the anodic current passage. Five times infiltration of LNO (which had the best achievement among other loadings of LNO; denoted as 5D in the figure) diminished the drastic increase of the resistance associated with the low-frequency peak during anodic polarization. Under catholic current passage of +200 mA cm^{-2}, Fig. 4c, the pure LSM low-frequency peak moved toward higher frequencies and depressed in a way that the peak was no longer detectable after 10 h. This similarly happened to the high-frequency peak. After infiltration of LNO nanoparticles, the peak of high frequencies remained unchanged, while the low-frequency related peak shifted toward lower frequencies and became taller, which leaded to the increase in overall polarization resistance.

In an study [82], Zhao et al. analyzed the electro-catalytic oxygen evolution reaction mechanism of $Ce_{0.9}Co_{0.1}O_{2-\delta}$-loaded LSM-YSZ oxygen electrodes (with four different amounts of $Ce_{0.9}Co_{0.1}O_{2-\delta}$) under 50% absolute humidity of H_2 and H_2O and OCV condition at 700–800 °C, using DRT method. The method was applied to analyze the EIS results of single-cell as well as stack. The team interpreted DRT results by considering the variation of EIS data with temperature, electrode materials, and some other results published in other studies [5,20,83,84]. As shown in Fig. 5a, there were five processes taking place at the air electrode, which were named P1-P5. It was reported that P1 is related to incorporation/evolution of O_2^- at electrolyte/ fuel electrode interface, P2 is related to charge transfer process in fuel electrode, P3 is for oxygen surface diffusion, P4 is for charge transfer reaction at oxygen electrode,

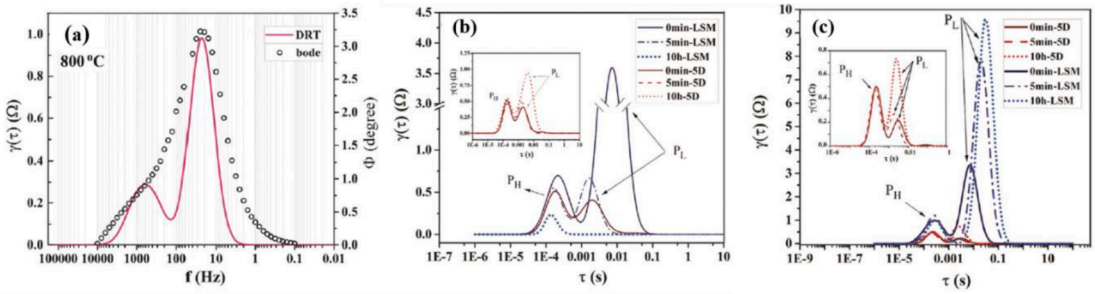

Fig. 4. (a) a comparison between DRT and bode curves of pure LSM at 800 °C under OCV (b) DRT plots of pure LSM and five-time LNO-infiltrated LSM under the anodic current passage of −200 mA cm^{-2} at 800 °C for 10 h, (c) DRT plots of pure LSM and five-time LNO-infiltrated LSM under the cathodic current passage of +200 mA cm^{-2} at 800 °C for 10 h [77].

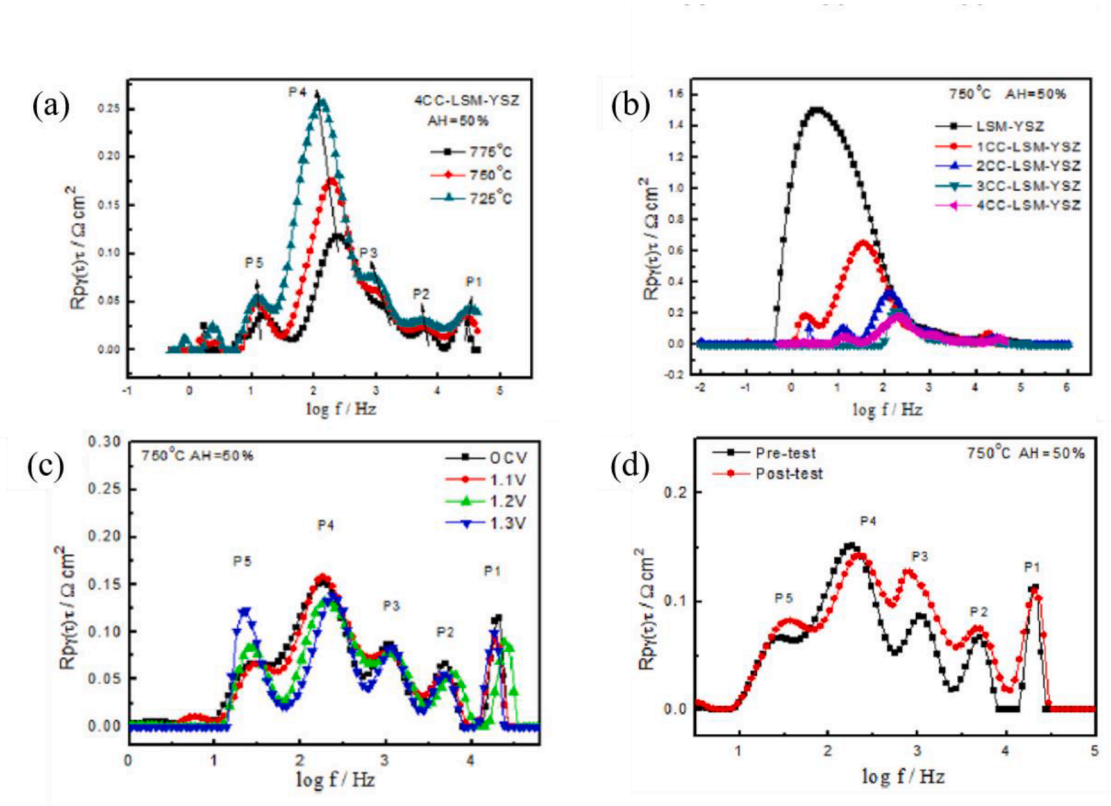

Fig. 5. (a) DRT spectra of $Ce_{0.9}Co_{0.1}O_{2-\delta}$ infiltrated LSM-YSZ at 725–775 °C under absolute humidity of 50%, (b) Dependence of DRT on the oxygen electrode, (c) DRT patterns of oxygen electrodes at various voltages, (d) DRT results of the $Ce_{0.9}Co_{0.1}O_{2-\delta}$ infiltrated LSM-YSZ cell before and after degradation testing [82].

and P5 is attributed to the diffusion process of H_2/H_2O in supported Ni-YSZ and Ni-YSZ fuel electrode. According to Fig. 5b, by adding $Ce_{0.9}Co_{0.1}O_{2-\delta}$ nanoparticles, P4 was reduced and this was related to the more surface oxygen vacancies of $Ce_{0.9}Co_{0.1}O_{2-\delta}$ on the LSM-YSZ scaffold and its higher lattice oxygen mobility. As seen in Fig. 5c, H_2/H_2O gas diffusion peak (P5) became larger when the electrolysis voltage increased from 1.1 to 1.3 V at 750 °C. This revealed that the process could become the key limiting factor for the SOEC performance at high electrolysis voltage. In the mentioned study, the team applied the DRT method to analyze the degradation mechanism, Fig. 5d Results of DRT spectra before and after a 120 h test illustrated some changes in P3, the peak associated with oxygen surface diffusion, which became larger and also shifted to lower frequencies. This phenomenon was related to the agglomeration of $Ce_{0.9}Co_{0.1}O_{2-\delta}$ nanoparticles on the oxygen electrode surface.

Shahrokhi et al. [85] analyzed the electrochemical behavior and the stability of $La_2Ni_{0.5}Co_{0.5}O_4$ (Ruddlesden-Popper) and $LaNi_{0.5}Co_{0.5}O_3$ (perovskite)-infiltrated $La_{0.8}Sr_{0.2}MnO_3$ air electrode under cyclic solid oxide electrolysis cell and solid oxide fuel cell modes. The group used the DRT approach as assistance to study the impact of the different loadings of Ruddlesden-Popper-structured LNC (which acted more effectively in comparison to the perovskite-structured nanoparticles) on the electrochemical performance of LSM. As for anodic polarization, there were three peaks on the DRT spectra, and the height of the peaks was lowered by increasing the loading of LNC nanoparticles, which was in agreement with the decreased polarization resistances obtained from EIS data. For the cathodic polarization, on the other hand, there was no order in the changes in the height of the peaks which decreased by one-time infiltrations and then increased with two and three-time infiltration, which proves the EIS results as well.

3.3. Lanthanide nickelates-based electrodes

The layered lanthanide nickelate oxides with the chemical formula of $Ln_{n+1}Ni_nO_{3n+1}$ (Ln = La, Pr, and Nd) are classed as Ruddlesden-Popper perovskites. This series of oxides show excellent oxygen bulk diffusion and surface exchange coefficients, and extraordinary oxygen ion conductivity by which they are regarded as one of the applicable electrode materials to SOC devices with an encouraging performance [86–88]. In a research study, Antonova et al. [89] employed the mixed conducting $La_2NiO_{4+\delta}$ (LNO) as the cathode material of SOFC and analyzed its electrochemical performance with two different thicknesses. In this study, the impedance spectra at 800 °C exhibited an asymmetric shape and it was claimed that this was denotative of several contributions to the overall cathode performance. To find the best fitted equivalent circuit they examined the impedance data via one or two *RQ* sub-circuits and a Gerischer element. The one which had the minimum error was an equivalent circuit with two *RQ* circuits for high and medium frequencies and a Grischer element for the low-frequency sub-process. Further DRT analysis revealed that the *(RQ)(RQ)(Ge)* fitting had the best match with experimental data and hence it was understood that there would be at least three relaxation processes. Based on the oxygen partial pressure dependency of the resistances of each sub-process, it was found that the high-frequency associated process had weak pO_2 dependency and this process was considered to be a process with a diffusive nature such as oxygen ion diffusion on the electrode/electrolyte interface. As for the medium-frequency process, based on pO_2-dependency, the charge transfer in the adsorption layer was regarded as the rate-limiting step. It was asserted that the parameters of Gerischer-type impedance in Eq. (2) are related to parameters that can characterize the processes happening in the material. Accordingly, the Gerischer admittance, Y_0, is representative of the oxygen diffusion coefficient and was independent of oxygen pressure, also the Gerischer time constant, K_G, is related to the oxygen interphase exchange rate and increased with oxygen pressure. In the mentioned study, the obtained results were compared with results of the oxygen isotopic exchange method with gas-phase equilibration for LNO which is done in another work [90]. The results of this method revealed that the oxygen diffusion coefficient did not change through oxygen partial pressure, while there

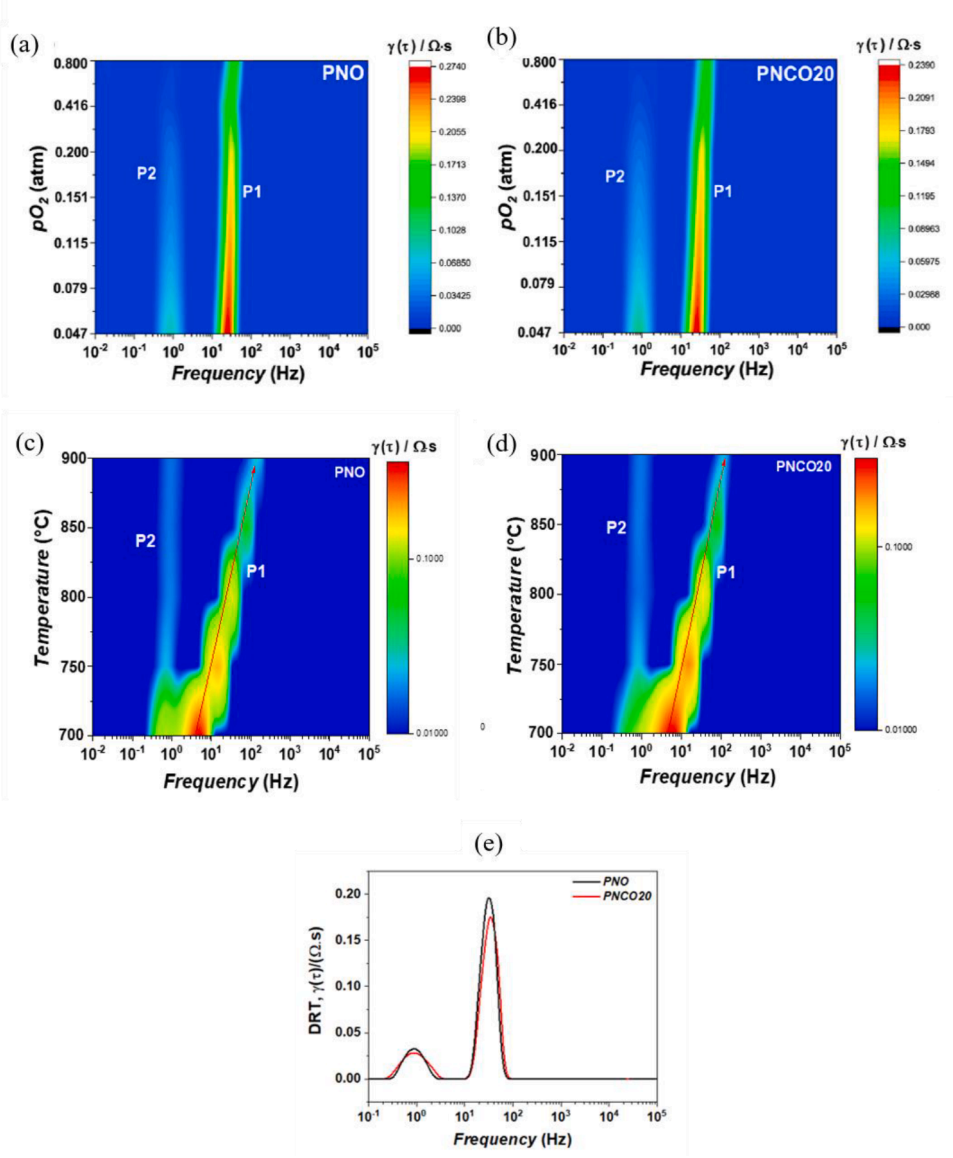

Fig. 6. DRT graph of (a) PNO (b) PNCO20 symmetric half-cells as a function of oxygen partial pressure cells at 800 °C under OCV conditions, and (c) PNO (d) PNCO20 symmetric half-cells as a function of temperature in air atmosphere under OCV condition, (e) PNO and PNCO20 symmetric half-cells at 800 °C under OCV condition in the air [72].

was a power-law dependence for oxygen surface exchange. Therefore, based on the correlation between the obtained results of this method and those found in the explained study, the low-frequency process represented by the Gerischer element was ascribed to oxygen surface exchange and oxygen diffusion.

$$R_{chem} = \frac{1}{Y_0\sqrt{K_G}} \quad (2)$$

To find an alternative air electrode for SOEC devices, Vibhu et al. [72] studied the electrochemical activity of the cobalt substituted $Pr_2Ni_{1-x}Co_xO_{4+\delta}$ (PNO) nickelate oxides in three different compositions with x values of 0, 0.1, and 0.2. Through this work, the enhancement of physicochemical properties, electrochemical performance, and durability of SOEC was achieved. To analyze the electrochemical response and determine the rate-limiting step of the PNO and PNCO20 ($x = 0.2$), the group examined various impedance spectra with the variation of oxygen partial pressure at 800 °C and it was seen that with decreasing the oxygen partial pressure, an increase in polarization resistance happened. Through a 3D-DRT analysis, as it is shown in Fig. 6a and b, two peaks were detected around the frequencies of 1–100 Hz (P_1) and 1 Hz (P_2) which were independent of cobalt content. The resistance corresponding to each peak decreased with the increase of oxygen partial pressure and P_1 had always higher values of resistance. Apart from that, with the increase of oxygen partial pressure, there was a slight shift towards higher frequencies for P_1. Another 3D-DRT analysis as a function of temperature, Fig. 6c and d, was performed. Based on that although the resistance and peak position corresponding to P_2 remained independent with the increasing temperature, not only did P_1 shift toward higher frequencies, but also it showed activation with increasing temperature. The peaks also merged at lower temperatures, mostly at 700 °C. Based on the DRT results, an equivalent circuit with two RQ elements and a series resistance, R_s, was applied to determine the resistances of two sub-processes corresponding to two peaks. The values were then confirmed through the integral area DRT peaks. Despite the constant values of P_2, 0.01 Ω.cm^2, for both PNO and PNCO20 oxygen electrodes, the values of P_1 decreased with increasing the temperature from 700 to 900 °C. According to the power-law relationship between the resistance of each process and oxygen partial pressure($R_p = R_p^0 (P_{O_2})^{-n}$), the values of 0.25 and 1 were obtained as the slope of the R_p-pO_2 diagram at the temperature of 800 °C for both PNO and PNCO20 symmetric half-cells. The 0.25 value was related to oxygen surface exchange reaction i.e. charge transfer process (surface diffusion of the adsorbed/desorbed oxygen atoms and their further reduction/evolution) and the 1 value was related to the gas diffusion process. Since the values and the corresponding processes were the same for both electrodes, it was reported that the substitution of cobalt at the nickel site did not have any impact on electrode sub-processes. It should be pointed out that the resistance related to P_1 was always higher than the other ones in all the ranges of oxygen partial pressures, and the charge transfer process was considered to be the rate-limiting step.

3.4. BSCF-based electrodes

Perovskite oxide (Ba,Sr)(Co,Fe)O_3 (BSCF) is known as one of the most active MIEC oxygen electrode materials whose enhanced electrocatalytic activity toward ORR is attributed to its excellent oxygen vacancies concentration and oxygen diffusion rate [91,92]. In a study about the BSCF cathode electrode of microtubular SOFC, Sumi et al. [91] optimized the sintering temperature of this material to prevent the formation of (Ba,Sr)ZrO_3 as an excessive unwanted phase created by the reactivity of BSCF and commonly used YSZ electrolyte. The impedance spectra corresponding to the electrochemical response of BSCF material, which was sintered at 900 °C (and there was no reaction between YSZ and BSCF at this sintering temperature), contained several overlapped processes owing to the components of both cathode and anode electrodes. To separate each sub-process, the DRT approach was applied. Accordingly, five peaks were detected. Two peaks at the frequencies of 2–3 and 0.6–0.9 kHz were representative of the fuel oxidation process at the fuel electrode or anode. At the frequencies of 20–30 and 10–20 Hz, there were two peaks ascribed to the oxygen electrode, namely the ion diffusion process in the MIEC conductor and the oxygen exchange process on the surface of the electrode, respectively. Also, it was reported that gas leakage might affect the diffusion polarization of the fifth peak in the DRT graph (< 3 Hz). The DRT results of the BSCF electrode were compared with the DRT results of the LSCF electrode sintered at the same temperature. The outcomes revealed that the resistance associated with the oxygen exchange process at the cathode for BSCF was smaller than that of LSCF at temperatures of 625–700 °C suggesting that BSCF sintered at 900 °C shows better electrochemical activity than conventional LSCF. The sintering temperature therefore is a pivotal criterion to achieve a high-performance BSCF electrode, as the BSCF electrode sintered at a higher temperature did not act as well as the one sintered at 900 °C. In another work, Clematis et al. [92] combined potential BSCF with the conventional LSCF in three different volume ratios (BSCF-LSCF 50–50 v/v%: BL50, BSCF-LSCF 70–30 v/v%: BL70, and BSCF-LSCF 30–70 v/v%: BL30) to generate an active cathode material for SOFCs at the temperature range of 500–650 °C. Analysis of the Nyquist plots of each three samples (Fig. 7a) revealed that the polarization resistances remarkably decreased, compared with pure LSCF and BSCF. Among the three above-mentioned samples, BL70 had the least polarization resistance and the shape of its plots corresponding to each temperature was different; suggesting that both the polarization resistance and all the mechanism happening at the electrode were affected by temperature and this fact was confirmed by examining DRT graphs at OCV. DRT approach was chosen as an alternative for the equivalent circuit model. This is due to the fact that the introduction of a unique equivalent circuit for all spectra at various temperatures was impossible, as the system was non-trivial. Besides, through this DRT approach, it would be possible to study the kinetic changes at different temperatures. Looking at Fig. 7b, the shape of DRT spectra at 500 °C consisted of the main peak at low frequencies around 10 Hz and a tail at medium-high frequencies which was representative of a typical Gerischer behavior indicating that the system was co-controlled by oxygen surface exchange and bulk diffusion processes. An R_1G equivalent was subsequently used to fit the impedance data and confirm the Gerischer hypothesis; R_1 is ohmic resistance and G is the Gerischer element. When the temperature is increased to 600–650 °C, as it is shown in Fig. 7b, a shift was seen for the main peak from low to high-medium frequencies (around 140 Hz) plus a significant decrease in the area under the peak. This revealed the kinetic mechanism enhancement and the thermal activation of the process. In addition to this, in these higher temperatures, a second peak was also detected at lower frequencies (around 1 Hz), which was attributed to the surface processes such as oxygen adsorption or oxygen gas diffusion. At 650 °C, in comparison with 600 °C, in spite of the fact that total resistance decreased, the low-frequency peak experienced an increase in the height of the peak and shifted toward lower frequencies which was doubtfully ascribed to unfavorable oxygen adsorption on the electrode surface or partial surface coverage; however, it was mentioned that this could not simplistically nominate because of the complexity of the system. DRT showed the changed kinetic at higher temperatures and an equivalent circuit of $R_1(R_{HF}Q_{HF})(R_{LF}Q_{LF})$ was applied to fit the obtained data at the given temperatures. In further investigations, the group reported various impedance data and corresponding DRT plots under cathodic polarization with various cathodic overpotentials at the temperatures of 500 and 650 °C for BL30 and BL70 samples. Extrapolation of the amounts of various elements of equivalents circuits of both BL70 and BL30 confirmed the Grischer element introduced by DRT for samples at 500 °C. What is more, the values of high and low-frequency resistances and the high and low-frequency capacitances (calculated from CPE parameters) were reported as a function of overpotential and the outcomes showed at 650 °C the medium-high frequency process is the

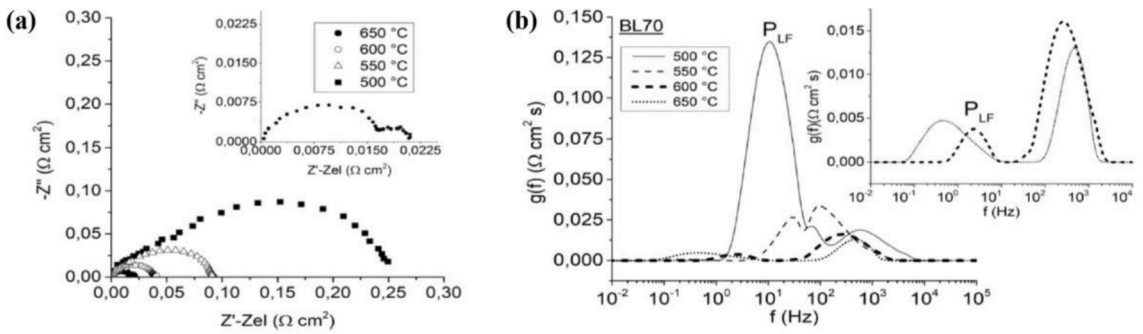

Fig. 7. (a) Impedance spectra and (b) DRT graphs for BL70 sample at OCV in the temperature ranges of 500–650 °C [92].

rate-limiting step; as suggested by DRT plots.

3.5. Double perovskites

Double perovskites with the chemical formula of AAB_2O_6 (called double A site) or A_2BBO_6 (called double B site) have gained much attention as the air electrode of SOFC and SOEC devices. This is while, there are not considerable number of papers using DRT approach in the electrochemical analysis of this group of material; yet, in this section we will cover some recent works taking advantage of this technique in their research. Zare et al. [93] studied the electrochemical performance of $Sr_2Fe_{1.5}Mo_{0.5}O_{6-\delta}/Ce_{0.9}Gd_{0.1}O_{1.95}$ composites as the cathode material of SOFCs, which were in the half-cell configuration of SFM/GDC|GDC|YSZ|GDC|SFM/GDC where YSZ was the electrolyte, and GDC served as the interlayer preventing unwanted reactions. After finding the optimum sintering temperature of the electrodes (1050 °C), the group searched for the electrochemical sub-processes of the cathode via DRT. What is interesting about the approach of the group is that they used DRT and CNLS fitting as two coupling methods to interpret the EIS data; this is different from the work of many researchers who applied DRT as a guidance towards finding an ECM. In fact, as shown in Fig. 8b, they observed three DRT peaks for the samples tested at 650 °C which were at the frequencies of 1, 100, and 2000 Hz. While seeing three DRT peaks should have resulted to an ECM with 3 RQ elements, the fitting results with this type of circuit were not satisfying enough. The group then tested an ECM with a Grischer element ($LR(R_HQ)G$) which showed good fitting results. Based on the Fig. 8b, P3 was the peak observed at high-frequency ranges (i.e. 2000 Hz), and it showed a charge transfer process at the interface of electrode and electrolyte. P1 and P2 on the other side were the peaks of lower frequencies part of the spectra which were ascribed to the Grischer element, and they represented diffusion and surface exchange processes. Also, that P1 and P2's height were decreased by heightening temperature and that they merged at 800 °C (as shown at Fig. 8b) were attributed to the thermal activation of oxygen diffusion and surface exchange processes at higher temperatures. It is worth mentioning that the group analyzed the values of R_H and R_G by equivalent circuit model and followed their changes through rising the temperature. Zhang et al. [94] introduced a dual-phase material being $PrBaCo_2O_{5+\delta}$ and $Gd_{0.1}Ce_{0.9}O_{2-\delta}$ as a potential cathode for intermediate-temperature SOFCs with high oxygen reduction reaction activity. The group firstly investigated electrical conductivity relaxation of electrodes with different loadings of GDC (0, 10, 20 and 30 wt%) and realized that the addition of GDC led to fast oxygen exchange process. They then employed EIS to study the oxygen reduction reaction process and found that the one containing10 wt% GDC had the best electrochemical performance. The whole oxygen reduction reaction was regarded to be made from six sub-processes for each of which an special value of m was considered based on the relationship of polarization resistance and oxygen partial pressure ($R_p = R_P^0 (P_{O_2})^{-m}$). The sub-reactions were adsorption of gaseous oxygen on the electrode surface ($m = 1$), dissociation of gaseous oxygen on the cathode surface ($m = 1/2$), reduction of oxygen atoms capturing one electron ($n = 1/8$), capturing another electron by partially reduced oxygen ($m = 1/8$), combination of adsorbed oxygen ions with oxygen vacancies in the lattice ($m = 0$), and transportation of oxygen ions at the interface of electrode and electrolyte ($m = 0$). It is worth mentioning that since some of the mentioned steps are too fast to be observed, all of the sub-reactions cannot be rate-limiting processes of a material. Considering the relationship of polarization resistance and oxygen partial pressure and the EIS of PBC-10 wt% GDC at the temperatures of 650, 750, and 850 °C and at four oxygen partial pressures, the group went for DRT analysis. The DRT spectra of all temperatures revealed four distinct peaks namely P1 with the frequency of tens of thousands Hz, P2 with the frequency of thousands Hz, P3 with the frequency of hundreds Hz and dozens, and P4 with the frequency of several Hz (shown in Fig. 9b for 750 °C). Based on Fig. 9b, with an increase in oxygen partial pressure, all peaks got smaller and shifted to higher frequencies, meaning rapid

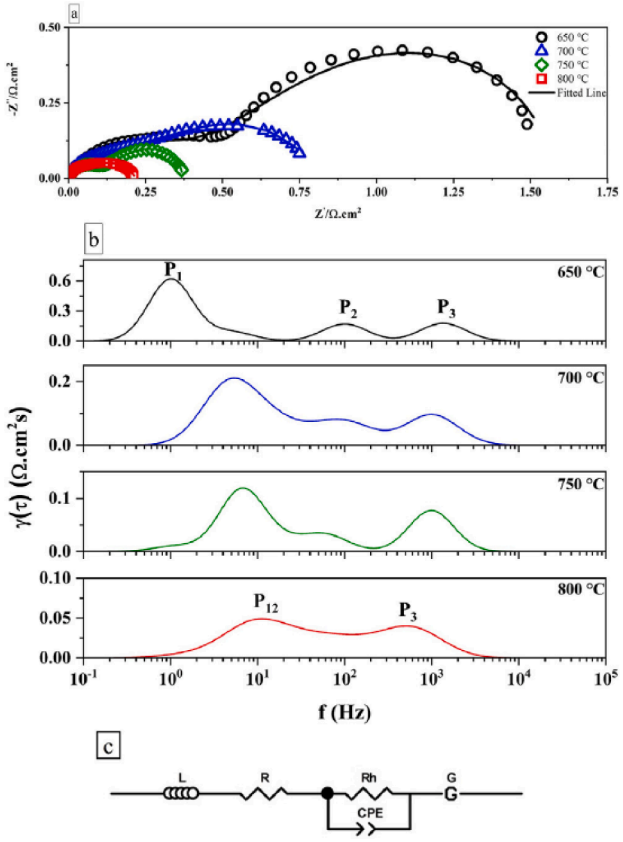

Fig. 8. (a) EIS plots, (b) DRT curves corresponding to the EIS spectra of SFM/GDC electrode, and (c) equivalent circuit [95].

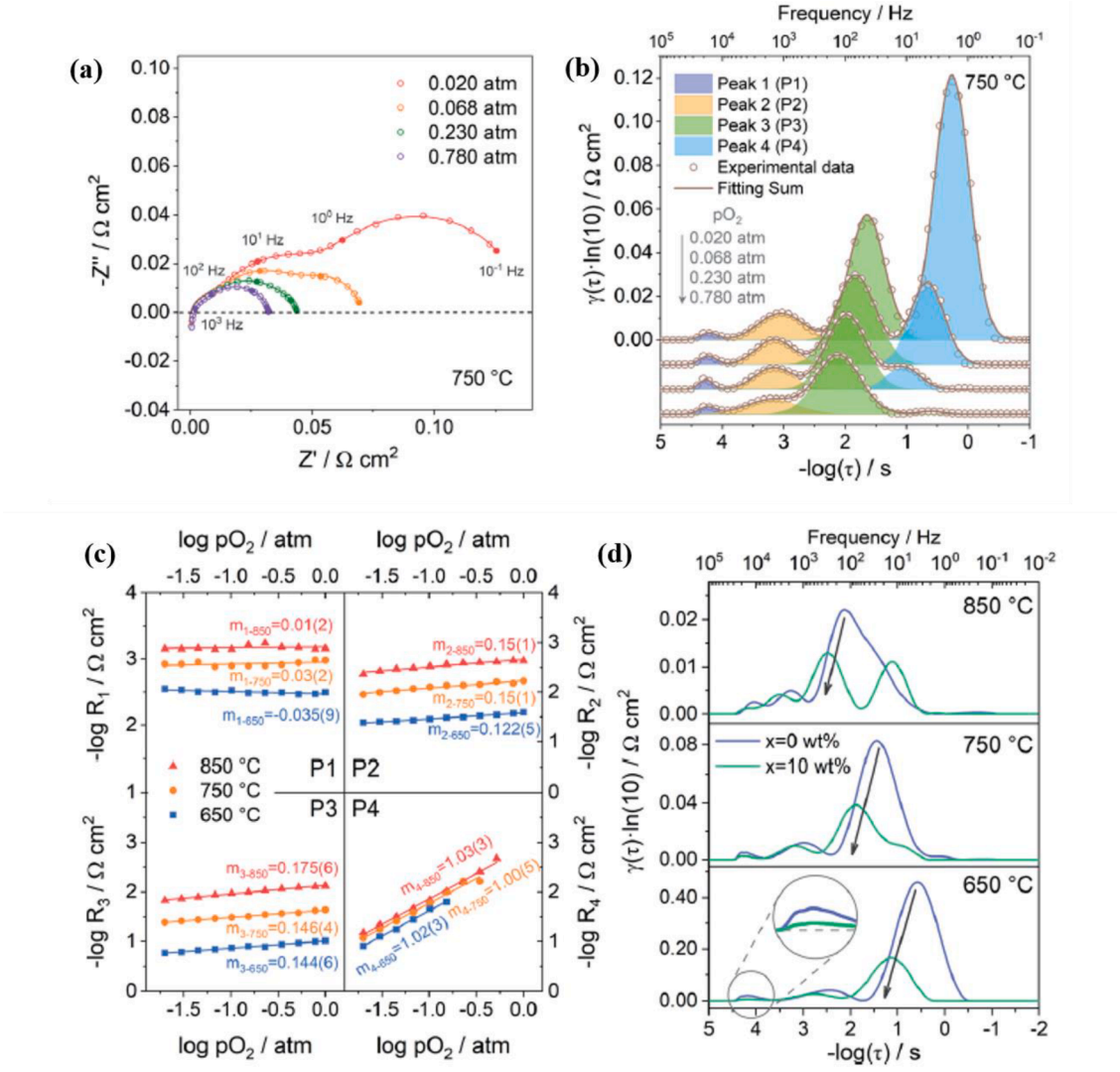

Fig. 9. (a) Nyquist plots of PBC-10 wt% GDC under different oxygen partial pressures and at 750 °C, (b) Corresponding DRT spectra, (c) polarization resistance of the DRT peaks as a function of oxygen partial pressure, and (d) DRT spectra of PBC- xwt% GDC with $x = 0$ and $x = 10$ [94].

kinetics. By considering the relationship between the integral area under each peak of DRT and oxygen partial pressure (Fig. 9c), the processes associated with peaks were found. Accordingly, for P1, *m* was 0, showing that the peak was independent of oxygen partial pressure, and since the peak had the highest frequency, it was attributed to oxygen ions transport across the interface of electrode and electrolyte. P2 and P3 were representative of similar processes, for they had the same value of *m* that was close to 1/8 and related to partially reduced oxygen atoms which had received one electron. Concerning P4, *m* was 1, showing the process of oxygen gaseous adsorption on the electrode surface. What is more, as P1 was remarkably small, they deduced that there had been good interface contact and fast oxygen ion transport between the electrode and the electrolyte which was LSGM. Another point found from DRT method was that since increasing the oxygen partial pressure typically accelerates electrochemical reactions, the large size of P2 and P3 peaks at oxygen partial pressure of 0.230 atm (Fig. 9b), which is close to air condition, revealed the rate-limiting step for the PBC-10 wt% GDC electrodes was charge transfer. When understanding each peak, the group again took advantage from DRT to find a way by which GDC bettered the performance of electrodes. As seen in Fig. 9d, compared with an electrode with 0 wt% GDC, the peak with the characteristic frequency of hundreds of Hz (P3) fell remarkably by the addition of 10 wt% GDC, which confirmed that GDC had improved charge transfer sub-reactions.

3.6. Other electrode materials

Although the vast majority of studies using the DRT approach have worked on common electrode materials, there are some reports on others. In a fuel cell containing a supporting electrode and a film electrolyte, both cathodic and anodic reactions are represented in the impedance spectra. Separating these reactions in the spectra is mostly difficult because of the fact that manufacturing a reference electrode is problematic as its potential will depend on the potential of the cathode and anode [26]. D.A. Osinkin [26] used the DRT approach to solve this problem. To do this, five types of electrochemical cells were used including three fuel cells with a supporting nickel-ceramic anode- cell 1: Ni-$Zr_{0.84}Y_{0.26}O_{1.9}$ (the support layer) / Ni-$Zr_{0.83}Sc_{0.26}Ce_{0.01}O_{1.92}$ (the functional layer) / $Zr_{0.84}Sc_{0.16}O_{1.92}$ (the electrolyte) / Pt-$Zr_{0.84}Y_{0.16}O_{1.92}$ (the cathode); cell 2: cell 1 + Pr_6O_{11} on the cathode; cell 3: cell 2 + CeO_2 on the anode– and two cells with a supporting electrolyte and symmetrical cathode electrodes– cell 4: Pt-$Zr_{0.84}Y_{0.16}O_{1.92}$ (the cathode) / $Zr_{0.84}Sc_{0.16}O_{1.92}$ (the electrolyte) / Pt-$Zr_{0.84}Y_{0.16}O_{1.92}$ (the cathode); cell 5: cell 4 + Pr_6O_{11} on the cathodes. Firstly, to assure that the DRT results are reliable, two methods were considered to obtain the DRT spectra. The first one was the traditional method of calculating the DRT functions

for which knowing the value of the regularization parameter is necessary. Since, there are no completely reliable mathematical approach to determine the exact value of regularization parameter, the second method that did not need the adjustment of this parameter was applied. The details of the second approach are reported in [22,43]. Fig. 10a illustrates the results of the first approach for various regularization parameters for the experimental impedance spectra of cell 2 at 900 °C, which shows that the number of peaks was increasing with decreasing the value of the regularization parameter. On the other hand, based on the second approach as shown in Fig 10b, seven peaks were revealed on the DRT spectra, which had a good correlation with the DRT result obtained at the regularization parameter of 0.01 from the first approach. According to these results, it was deduced that the electrochemical response of the cell 2 could be determined with seven peaks or sup-processes. To differentiate anodic reactions from cathodic ones, the DRT curves of fuel cell 1 was analyzed first, in which the peak with the maximum intensity and area contained 75% of the whole polarization resistance (based on the area under each peak that equals the polarization resistance) and had little changes with the variation of the partial pressure of hydrogen in a wet H_2/Ar mixture (cathode under air), Fig. 10c The DRT functions of symmetrical electrodes (cell 4) were then analyzed, Fig. 10c Results showed that the aforementioned peak was also visible in the DRT spectra of the symmetrical cell and coincided with it, confirming the fact that the electrochemical activity of fuel cell 1 was mainly limited by the cathode. The stability of the peak under a partial pressure of hydrogen was a confirmation of this result as well. The DRT functions of the fuel cell 2 and symmetrical cell 5 were also compared at different temperatures and different partial pressure of hydrogen (at the anode) and oxygen (at the cathode), Fig. 10d Comparing the results, it is possible to unambiguously distinguish between the cathodic reactions and anodic ones as symmetrical cell 5 completely shows the cathodic reactions of fuel cell 2. The changes of the peaks under oxygen or hydrogen partial pressures in Fig. 10d can nicely show the location of cathodic and anodic peaks.

Apart from that, the addition of praseodymium oxide to fuel cell 1 (fuel cell 2) caused higher power density and since the DRT function of symmetrical cell 4 (without praseodymium oxide) was greatly similar to the DRT function of cell 5 (with praseodymium oxide) – the peaks relaxed at the same frequency range – it was understood that the addition of the oxide had not changed the mechanism of the cathode but its rate (the rate of interfacial exchange of oxygen between the air electrode and the gas phase). It is noteworthy that the addition of ceria to the anode had no significant impact on cathodic reactions but changed the behavior of anodic processes which was realized by comparing the DRT functions of the fuel cell 2 (without ceria) and fuel cell 3 (with ceria).

Li et al. [96] studied the electrocatalytic performance of $Ba_{0.95}La_{0.05}Fe_{0.9}Nb_{0.1}O_3$ (BLFN) toward the oxygen reduction and hydrogen reduction reaction as the cathode and anode of the symmetrical solid oxide fuel cells. They used the DRT method to understand the electron reaction process under different oxygen and hydrogen partial pressures and temperatures. Here we only focus on its behavior as the cathode material. DRT curves obtained from the EIS data under OCV conditions, different oxygen partial pressures (0.21, 0.10, 0.05, 0.025 atm), and 750 °C revealed two characteristic peaks in the low-frequency range (1–10 Hz), and the high-frequency range (100–1000 Hz). Decreasing the P_{O2} from 0.21 to 0.025 increased the intensities of both peaks, which showed that the two sub-processes were closely related to the gas concentration. Based on the appearance of the two sub-steps of the electrode, the EIS data were fitted with the equivalent circuit of $LR_{ohm}(R_{LF}Q_{LF})$ $(R_{HF}Q_{HF})$. The group calculated the polarization resistances of both R_{LF} and R_H through DRT peak areas and the equivalent circuit fitting method, where small differences were reported between the results. Based on the relationship between polarization resistances and P_{O2} ($R_p = R_P^0 (P_{O_2})^{-n}$), the low-frequency sub-step was related to the molecular oxygen adsorption and diffusion at the electrode surface, and the high-frequency sub-step was related to the dissociation of

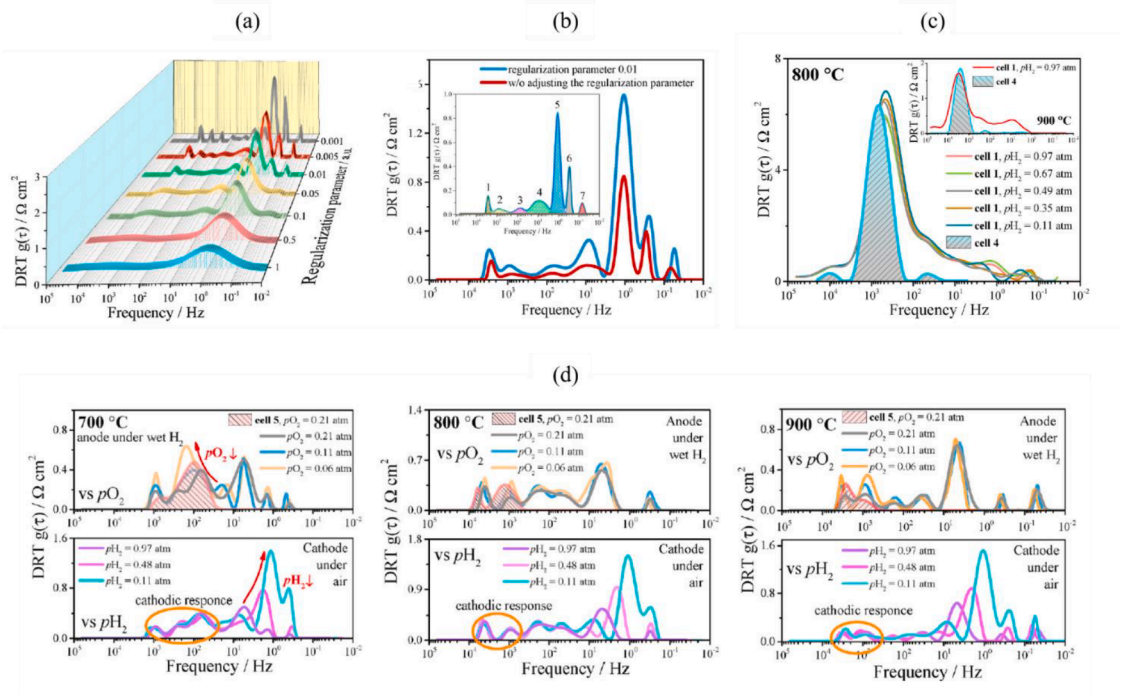

Fig. 10. (a) DRT functions based on different values of regularization parameter (b) DRT functions calculated with the regularization parameter of 0.01 and without adjustment of the regularization parameter (the insert shows an example of determining the area under each peak) (c) DRT function of the fuel cell (cell 1) at different partial pressures of hydrogen in a wet mixture of H_2/Ar (cathode was under air) and DRT function of the symmetrical cathodic cell (cell 4) under air at 800 °C (the insert is the DRT functions of the fuel cell (cell 1) and the symmetric cell (cell 4) under air at 900 °C (d) DRT functions of the fuel cell (cell 2) at a different partial pressure of hydrogen in a wet mixture of H_2/Ar for the anode and different partial pressure of oxygen for the cathode at various temperatures and DRT functions of the symmetrical cathodic cell (cell 5) under air [26].

surface-adsorbed oxygen. Since the R_{HF} was larger than R_{LF}, the dissociation of surface-adsorbed oxygen was the rate-limiting step of the BLFN cathode.

6. Concluding remarks

The main goal of the DRT technique is to elaborate the physicochemical mechanisms of electrochemical devices by identifying the characteristic distribution of EIS time scales. Another plus point of this method is its ability to detect overlapped phenomena involved in EIS data. Moreover, in the case of matters for which there is no prior knowledge about their electrochemical performance, DRT approach can shed light on their behavior. In this paper, we reviewed various studies which employed DRT as the main or additional technique of analysis to assess the performance of the most common SOFC/SOEC's air electrodes, as well as some less-common onesBy considering the approaches of the reviewed scientific reports, it can be deduced that DRT can be applied in various ways. In fact, as it was reviewed, to achieve a reliable investigation, employing DRT in various operating parameters such as different temperatures, different oxygen partial pressures, various current densities, varied time, and several loadings of introduced materials is necessary. Since obtaining a univocal DRT is challenging, changing operating parameters can ensure the researchers about the exact DRT corresponding to the system under study. Studying the processes would also be more precise by tracing the DRT obtained in various operating parameters. In addition, it was shown that DRT can give valuable information about the degradation mechanism, changing the shapes of Nyquist plots, varying kinetic regimes, and so on. Driving from these, the DRT approach is regarded as a rather new way to analyze electrochemical systems more accurately and comprehensively than the equivalent circuit model conventional method. Needless to say that the method needs some improvements in order that it can be more trustworthy. For example, should future researchers work on a rigorous mathematical method for adjusting the regularization parameter, achieved results would be more reliable. At the end, we ought to recommend futures researchers to provide the details of the method by which they got their DRT results in their research papers. By doing so, the field will be developed sooner than it already does.

Declaration of Competing Interest

The authors declare that they have no known competing financial interests or personal relationships that could have appeared to influence the work reported in this paper.

Data availability

Data will be made available on request.

References

[1] M.B. Mogensen, Materials for reversible solid oxide cells, Curr. Opin. Electrochem. 21 (2020) 265–273.
[2] D. Huan, et al., New, efficient, and reliable air electrode material for proton-conducting reversible solid oxide cells, ACS Appl. Mater. Interfaces 10 (2) (2018) 1761–1770.
[3] H. Ding, Nanostructured Electrodes for High-Performing Solid Oxide Fuel Cells, in Nanostructured Materials for Next-Generation Energy Storage and Conversion, Springer, 2018, pp. 227–247.
[4] S.P. Jiang, Q. Li, Solid Oxide Fuel Cells: Techniques and Characterization, Introduction to Fuel Cells, Springer, 2022, pp. 497–560.
[5] X. Tong, et al., Large-area solid oxide cells with La0. 6Sr0. 4CoO3-δ infiltrated oxygen electrodes for electricity generation and hydrogen production, J. Power Sources 451 (2020), 227742.
[6] J. Zamudio-García, et al., A review on recent advances and trends in symmetrical electrodes for solid oxide cells, J. Power Sources 520 (2022), 230852.
[7] T.K. Das, A. Poater, Review on the use of heavy metal deposits from water treatment waste towards catalytic chemical syntheses, Int. J. Mol. Sci. 22 (24) (2021) 13383.
[8] T.K. Das, et al., Mussel-inspired Ag/poly (norepinephrine)/MnO_2 heterogeneous nanocatalyst for efficient reduction of 4-nitrophenol and 4-nitroaniline: an alternative approach, Res. Chem. Intermed. 46 (2020) 3629–3650.
[9] G. Kaur, Solid Oxide Fuel Cell Components, Springer, Switzerland, 2016.
[10] Z. Shao, M.O. Tadé, Intermediate-temperature solid oxide fuel cells, Chem. Soc. Rev. 37 (2016) 1568–1578.
[11] A.P. Tarutin, et al., Nickel-containing perovskites, $PrNi_{0.4}Fe_{0.6}O_3$–δ and $PrNi_{0.4}Co_{0.6}O_3$–δ, as potential electrodes for protonic ceramic electrochemical cells, Materials 15 (6) (2022) 2166 (Basel).
[12] M. Khan, et al., Air electrodes and related degradation mechanisms in solid oxide electrolysis and reversible solid oxide cells, Renew. Sustain. Energy Rev. 143 (2021), 110918.
[13] T.K. Das, N.C. Das, Advances on catalytic reduction of 4-nitrophenol by nanostructured materials as benchmark reaction, Int. Nano Lett. 12 (3) (2022) 223–242.
[14] T.K. Das, P. Ghosh, N.C. Das, Preparation, Development, Outcomes, and Application Versatility of Carbon Fiber-Based Polymer Composites: A Review, 2, Advanced Composites and Hybrid Materials, 2019, pp. 214–233.
[15] S.P. Jiang, Development of lanthanum strontium cobalt ferrite perovskite electrodes of solid oxide fuel cells-a review, Int. J. Hydrog. Energy 44 (14) (2019) 7448–7493.
[16] D. Ding, et al., Enhancing SOFC cathode performance by surface modification through infiltration, Energy Environ. Sci. 7 (2) (2014) 552–575.
[17] Y. Chen, et al., A highly efficient multi-phase catalyst dramatically enhances the rate of oxygen reduction, Joule 2 (5) (2018) 938–949.
[18] S.N. Sampathkumar, et al., Degradation study of a reversible solid oxide cell (rSOC) short stack using distribution of relaxation times (DRT) analysis, Int. J. Hydrog. Energy 47 (18) (2022) 10175–10193.
[19] A. Belotti, et al., The influence of A-site deficiency on the electrochemical properties of $(Ba_{0.9}5La_{0.05})$ 1-xFeO_3-δ as an intermediate temperature solid oxide fuel cell cathode, Int. J. Hydrog. Energy 47 (2) (2022) 1229–1240.
[20] J. Xia, et al., A perspective on DRT applications for the analysis of solid oxide cell electrodes, Electrochim. Acta 349 (2020), 136328.
[21] D. Klotz, et al., The distribution of relaxation times as beneficial tool for equivalent circuit modeling of fuel cells and batteries, ECS Trans. 41 (28) (2012) 25.
[22] Y. Zhang, et al., A high-precision approach to reconstruct distribution of relaxation times from electrochemical impedance spectroscopy, J. Power Sources 308 (2016) 1–6.
[23] V.F. Lvovich, Impedance Spectroscopy: Applications to Electrochemical and Dielectric Phenomena, John Wiley & Sons, 2012.
[24] D.D. Macdonald, Reflections on the history of electrochemical impedance spectroscopy, Electrochim. Acta 51 (8–9) (2006) 1376–1388.
[25] M. Ghamarinia, A. Babaei, C. Zamani, Electrochemical characterization of La_2NiO_4-infiltrated $La_{0.6}Sr_{0.4}Co_{0.2}Fe_{0.8}O_3$-δ by analysis of distribution of relaxation times, Electrochim. Acta 353 (2020), 136520.
[26] D. Osinkin, Detailed analysis of electrochemical behavior of high–performance solid oxide fuel cell using DRT technique, J. Power Sources 527 (2022), 231120.
[27] S. Rauf, et al., Electrochemical properties of a dual-ion semiconductor-ionic $Co_{0.2}Zn_{0.8}O$-$Sm_{0.20}Ce_{0.80}O_2$− δ composite for a high-performance low-temperature solid oxide fuel cell, ACS Appl. Energy Mater. 4 (1) (2021) 194–207.
[28] H. Schichlein, et al., System identification: a new modelling approach for SOFC single cells, ECS Proc. Vol. 1999 (1) (1999) 1069.
[29] B.A. Boukamp, Distribution (function) of relaxation times, successor to complex nonlinear least squares analysis of electrochemical impedance spectroscopy? J. Phys. Energy 2 (4) (2020), 042001.
[30] B.A. Boukamp, A. Rolle, Use of a distribution function of relaxation times (DFRT) in impedance analysis of SOFC electrodes, Solid State Ion. 314 (2018) 103–111.
[31] B.A. Boukamp, Derivation of a distribution function of relaxation times for the (fractal) finite length Warburg, Electrochim. Acta 252 (2017) 154–163.
[32] T.H. Wan, et al., Influence of the discretization methods on the distribution of relaxation times deconvolution: implementing radial basis functions with DRTtools, Electrochim. Acta 184 (2015) 483–499.
[33] D.V. Lopes, et al., Electrochemical reduction of hematite-based ceramics in alkaline medium: challenges in electrode design, Electrochim. Acta 327 (2019), 135060.
[34] M. Saccoccio, et al., Optimal regularization in distribution of relaxation times applied to electrochemical impedance spectroscopy: ridge and lasso regression methods-a theoretical and experimental study, Electrochim. Acta 147 (2014) 470–482.
[35] F. Ciucci, Modeling electrochemical impedance spectroscopy, Curr. Opin. Electrochem. 13 (2019) 132–139.
[36] E. Ivers-Tiffee, A. Weber, Evaluation of electrochemical impedance spectra by the distribution of relaxation times, J. Ceram. Soc. Jpn. 125 (4) (2017) 193–201.
[37] H. Schichlein, et al., Deconvolution of electrochemical impedance spectra for the identification of electrode reaction mechanisms in solid oxide fuel cells, J. Appl. Electrochem. 32 (8) (2002) 875–882.
[38] D. Klotz, A. Weber, E. Ivers-Tiffée, Practical guidelines for reliable electrochemical characterization of solid oxide fuel cells, Electrochim. Acta 227 (2017) 110–126.
[39] L. Almar, et al., Oxygen transport kinetics of mixed ionic-electronic conductors by coupling focused ion beam tomography and electrochemical impedance spectroscopy, J. Electrochem. Soc. 164 (4) (2017) F289.
[40] M. Hahn, et al., Optimized process parameters for a reproducible distribution of relaxation times analysis of electrochemical systems, Batteries 5 (2) (2019) 43.
[41] A. Weiß, et al., Distribution of relaxation times analysis of high-temperature PEM fuel cell impedance spectra, Electrochim. Acta 230 (2017) 391–398.

[42] A. Gavrilyuk, D. Osinkin, D. Bronin, The use of Tikhonov regularization method for calculating the distribution function of relaxation times in impedance spectroscopy, Russ. J. Electrochem. 53 (6) (2017) 575–588.
[43] A. Gavrilyuk, D. Osinkin, D. Bronin, On a variation of the Tikhonov regularization method for calculating the distribution function of relaxation times in impedance spectroscopy, Electrochim. Acta 354 (2020), 136683.
[44] C. Graves, RAVDAV Data Analysis Software, Version 0.9. 7, Technical University of Denmark, Roskilde, Denmark, 2012.
[45] Available from: 2020 https://www.rhd-instruments.de/en/products/software/relaxis/relaxis-drt.
[46] A. Leonide, et al., Evaluation and modeling of the cell resistance in anode-supported solid oxide fuel cells, J. Electrochem. Soc. 155 (1) (2007) B36.
[47] B.A. Boukamp, Fourier transform distribution function of relaxation times; application and limitations, Electrochim. Acta 154 (2015) 35–46.
[48] B.A. Boukamp, A. Rolle, Analysis and application of distribution of relaxation times in solid state ionics, Solid State Ion. 302 (2017) 12–18.
[49] V. Sonn, A. Leonide, E. Ivers-Tiffée, Combined deconvolution and CNLS fitting approach applied on the impedance response of technical Ni/ 8YSZ cermet electrodes, J. Electrochem. Soc. 155 (7) (2008) B675.
[50] J.P. Schmidt, et al., Studies on LiFePO4 as cathode material using impedance spectroscopy, J. Power Sources 196 (12) (2011) 5342–5348.
[51] H. Sumi, et al., AC impedance characteristics for anode-supported microtubular solid oxide fuel cells, Electrochim. Acta 67 (2012) 159–165.
[52] J. Illig, et al., Understanding the impedance spectrum of 18650 $LiFePO_4$-cells, J. Power Sources 239 (2013) 670–679.
[53] T. Ramos, M. Søgaard, M.B. Mogensen, Electrochemical characterization of Ni/ScYSZ electrodes as SOFC anodes, J. Electrochem. Soc. 161 (4) (2014) F434.
[54] S. Kazlauskas, et al., Electrical properties of YSZ and CaSZ single crystals, Solid State Ion. 231 (2013) 37–42.
[55] Y. Zhang, et al., Reconstruction of relaxation time distribution from linear electrochemical impedance spectroscopy, J. Power Sources 283 (2015) 464–477.
[56] T. Hörlin, Maximum entropy in impedance spectroscopy of non-inductive systems, Solid State Ion. 67 (1–2) (1993) 85–96.
[57] T. Hörlin, Deconvolution and maximum entropy in impedance spectroscopy of noninductive systems, Solid State Ion. 107 (3–4) (1998) 241–253.
[58] H.W. Engl, M. Hanke, A. Neubauer, Regularization of Inverse Problems, 375, Springer Science & Business Media, 1996.
[59] N. Schlüter, S. Ernst, U. Schröder, Direct access to the optimal regularization parameter in distribution of relaxation times analysis, ChemElectroChem 7 (16) (2020) 3445–3458.
[60] N. Schlüter, S. Ernst, U. Schröder, Finding the optimal regularization parameter in distribution of relaxation times analysis, ChemElectroChem 6 (24) (2019) 6027–6037.
[61] M.-B. Choi, et al., Interpretation of impedance spectra of solid oxide fuel cells: l-curve criterion for determination of regularization parameter in distribution function of relaxation times technique, JOM 71 (2019) 3825–3834.
[62] J.P. Tomba, M. de la Paz Miguel, C.J. Perez, Correction of optical distortions in dry depth profiling with confocal Raman microspectroscopy, J. Raman Spectrosc. 42 (6) (2011) 1330–1334.
[63] T. Correia, et al., Selection of regularization parameter for optical topography, J. Biomed. Opt. 14 (3) (2009), 034044–034044-11.
[64] S. Dierickx, A. Weber, E. Ivers-Tiffée, How the distribution of relaxation times enhances complex equivalent circuit models for fuel cells, Electrochim. Acta 355 (2020), 136764.
[65] B.A. Boukamp, A linear Kronig-Kramers transform test for immittance data validation, J. Electrochem. Soc. 142 (6) (1995) 1885.
[66] M. Schönleber, D. Klotz, E. Ivers-Tiffée, A method for improving the robustness of linear Kramers-Kronig validity tests, Electrochim. Acta 131 (2014) 20–27.
[67] B.A. Boukamp, Practical application of the Kramers-Kronig transformation on impedance measurements in solid state electrochemistry, Solid State Ion. 62 (1–2) (1993) 131–141.
[68] V. Subotić, et al., Detailed insight into processes of reversible solid oxide cells and stacks using DRT analysis, Energy Convers. Manag. 226 (2020), 113509.
[69] A. Esquirol, et al., Electrochemical characterization of $La_{0.6}Sr_{0.4}Co_{0.2}Fe_{0.8}O_3$ cathodes for intermediate-temperature SOFCs, J. Electrochem. Soc. 151 (11) (2004) A1847.
[70] N. Ni, C.C. Wang, S.J. Skinner, Synergistic effects of temperature and polarization on Cr poisoning of $La_{0.6}Sr_{0.4}Co_{0.2}Fe_{0.8}O_{3-\delta}$ solid oxide fuel cell cathodes, J. Mater. Chem. A 7 (15) (2019) 9253–9262.
[71] J.W. Lee, et al., Preparation of dense and uniform $La_{0.6}Sr_{0.4}Co_{0.2}Fe_{0.8}O_{3-\delta}$ (LSCF) films for fundamental studies of SOFC cathodes, J. Power Sources 190 (2) (2009) 307–310.
[72] V. Vibhu, et al., Cobalt substituted Pr2Ni1-xCoxO4+ δ (x= 0, 0.1, 0.2) oxygen electrodes: impact on electrochemical performance and durability of solid oxide electrolysis cells, J. Power Sources 482 (2021), 228909.
[73] P. Li, et al., Enhanced electrochemical performance of co-synthesized La_2NiO_4+ δ-$Ce_{0.55}La_{0.45}O_2$-δ composite cathode for IT-SOFCs, J. Alloy. Compd. 705 (2017) 105–111.
[74] Z. Pan, et al., Effect of $La_{0.6}Sr_{0.4}Co_{0.2}Fe_{0.8}O_{3-\delta}$ air electrode–electrolyte interface on the short-term stability under high-current electrolysis in solid oxide electrolyzer cells, J. Power Sources 378 (2018) 571–578.
[75] M. Nadeem, et al., PbO effect on the oxygen reduction reaction in intermediate-temperature solid oxide fuel cell, Int. J. Hydrog. Energy 45 (46) (2020) 25299–25306.
[76] A. Soltanizade, et al., Temperature dependency of activity of nano-catalysts on $La_{0.6}Sr_{0.4}Co_{0.2}Fe_{0.8}O_{3-\delta}$ cathode of solid oxide fuel cells, J. Appl. Electrochem. 49 (11) (2019) 1113–1122.
[77] Z. Akbari, A. Babaei, Electrochemical performance of $La_{0.8}Sr_{0.2}MnO_3$ oxygen electrode promoted by Ruddlesden-Popper structured La_2NiO_4, J. Am. Ceram. Soc. 103 (2) (2020) 1332–1342.
[78] J. Zamudio-García, et al., Influence of $Bi_{1.5}Y_{0.5}O_3$ active layer on the performance of nanostructured $La_{0.8}Sr_{0.2}MnO_3$ cathode, Appl. Nano 1 (1) (2020) 14–24.
[79] S.P. Jiang, Nanoscale and nano-structured electrodes of solid oxide fuel cells by infiltration: advances and challenges, Int. J. Hydrog. Energy 37 (1) (2012) 449–470.
[80] C. Su, et al., Effects of a YSZ porous layer between electrolyte and oxygen electrode in solid oxide electrolysis cells on the electrochemical performance and stability, Int. J. Hydrog. Energy 44 (29) (2019) 14493–14499.
[81] Y. Song, et al., Improving the performance of solid oxide electrolysis cell with gold nanoparticles-modified LSM-YSZ anode, J. Energy Chem. 35 (2019) 181–187.
[82] Z. Zhao, et al., High-performance oxygen electrode $Ce_{0.9}Co_{0.1}O_2$-δ-LSM-YSZ for hydrogen production by solid oxide electrolysis cells, Int. J. Hydrog. Energy 46 (50) (2021) 25332–25340.
[83] J. Yan, et al., Co-synthesized Y-stabilized Bi2O3 and Sr-substituted $LaMnO_3$ composite anode for high performance solid oxide electrolysis cell, J. Power Sources 319 (2016) 124–130.
[84] P. Hjalmarsson, et al., Influence of the oxygen electrode and inter-diffusion barrier on the degradation of solid oxide electrolysis cells, J. Power Sources 223 (2013) 349–357.
[85] S. Shahrokhi, A. Babaei, C. Zamani, Reversible operation of $La_{0.8}Sr_{0.2}MnO_3$ oxygen electrode infiltrated with Ruddlesden-Popper and perovskite lanthanum nickel cobaltite, Int. J. Hydrog. Energy 43 (52) (2018) 23091–23100.
[86] P. Ding, et al., Review on Ruddlesden–Popper perovskites as cathode for solid oxide fuel cells, J. Phys. Mater. 4 (2) (2021), 022002.
[87] A.P. Tarutin, et al., Recent advances in layered Ln_2NiO_4+ δ nickelates: fundamentals and prospects of their applications in protonic ceramic fuel and electrolysis cells, J. Mater. Chem. A (2020).
[88] E.Y. Pikalova, et al., Structure, transport properties and electrochemical behavior of the layered lanthanide nickelates doped with calcium, Int. J. Hydrog. Energy 43 (36) (2018) 17373–17386.
[89] E. Antonova, et al., EIS analysis of electrode kinetics for La_2NiO_4+ δ cathode in contact with $Ce_{0.8}Sm_{0.2}O_{1.9}$ electrolyte: from DRT analysis to physical model of the electrochemical process, J. Solid State Electrochem. 23 (4) (2019) 1279–1287.
[90] M. Ananyev, et al., Oxygen isotope exchange in $La_2NiO_{4\pm\delta}$, Phys. Chem. Chem. Phys. 18 (13) (2016) 9102–9111.
[91] H. Sumi, et al., Prevention of reaction between (Ba, Sr)(Co, Fe) O_3 Cathodes and Yttria-stabilized Zirconica electrolytes for intermediate-temperature solid oxide fuel cells, Electrochim. Acta 184 (2015) 403–409.
[92] D. Clematis, et al., Electrocatalytic activity of perovskite-based cathodes for solid oxide fuel cells, Int. J. Hydrog. Energy 44 (12) (2019) 6212–6222.
[93] A. Zare, et al., Electrochemical evaluation of $Sr_2Fe_{1.5}Mo_{0.5}O6$-δ/$Ce_{0.9}Gd_{0.1}O_{1.95}$ cathode of SOFCs by EIS and DRT analysis, J. Electroanal. Chem. (2023), 117376.
[94] Y. Zhang, et al., Enhanced oxygen reduction kinetics of IT-SOFC cathode with $PrBaCo_2O_5$+ δ/$Gd_{0.1}Ce_{1.9}O_2$− δ coherent interface, J. Mater. Chem. A 10 (7) (2022) 3495–3505.
[95] A. Zare, et al., Electrochemical evaluation of $Sr_2Fe_{1.5}Mo_{0.5}O6$-δ/$Ce_{0.9}Gd_{0.1}O_{1.95}$ cathode of SOFCs by EIS and DRT analysis, J. Electroanal. Chem. 936 (2023), 117376.
[96] Z. Li, et al., A novel $Ba_{0.95}La_{0.05}Fe_{0.9}Nb_{0.1}O_{3-\delta}$ ceramic electrode for symmetrical solid oxide fuel cells, Sustain. Energy Fuels 5 (23) (2021) 5975–5984.